LUNAR OLIVINE EXPOSURES: ORIGINS AND MECHANISMS OF TRANSPORT

A FINAL REPORT SUBMITTED TO THE DEPARTMENT OF GEOLOGY AND GEOPHYSICS, UNIVERSITY OF HAWAIʻI AT MĀNOA, IN PARTIAL FULFILLMENT OF THE REQUIREMENTS FOR THE DEGREE OF

MASTER OF SCIENCE

IN

GEOLOGY AND GEOPHYSICS

May 2016

By

Laura M. Corley

Advisor:

Jeffrey Gillis-Davis

Abstract

High-resolution hyperspectral data from Chandrayaan-1's Moon Mineralogy Mapper (M^3) allow detection of olivine. We identified 124 M^3 olivine spectra on rims and ejecta of small craters, basin rim massifs, and maria. Specifically these areas are Crisium, Nectaris, and Humorum basins and near the crater Roche. Olivine exposures at the surface may be mantle material, or shallow intrusions. Transport mechanisms include excavation of mantle or lower crustal material by basin-forming impacts, or magmatic emplacement of cumulates or xenoliths. In an effort to distinguish between structural or magmatic origin, we estimated mineral abundances using Hapke radiative transfer modeling and examined modeled crustal thickness from the Gravity Recovery Interior Laboratory (GRAIL) mission data. Maps of topography and slope, created using data from the Lunar Orbiter Laser Altimeter (LOLA), and Wide Angle Camera (WAC) and Narrow Angle Camera (NAC) images from Lunar Reconnaissance Orbiter (LRO) allowed for further observation of geologic settings. Integration of spectral, geophysical, and morphological data yields evidence for olivine excavated from the mantle at Crisium, as well as olivine transported magmatically at all four study areas. Our findings identify possible origins and transport mechanisms of exposed olivine, providing insight to the structural and magmatic evolution of the Moon.

Introduction

Although relatively rare in the lunar crust, olivine has been detected on the surface using high-resolution spectral data. Yamamoto et al. (2010) used data from KAGUYA's Spectral Profiler (SP) to identify olivine located on rims and central peaks of several large impact basins within areas of thinned crust. They concluded that the olivine spectra were from dunite, and thus likely originated in the upper mantle. Powell et al. (2012) examined Crisium basin using Chandrayaan-1's Moon Mineralogy Mapper (M^3) spectra. They detected olivine within mare deposits, intrusive landforms, and in areas of thick crust, and concluded that both magmatic and mantle olivine is present.

Basin-forming impacts may have excavated olivine that originated in the mantle or in Mg-suite plutons in the lower crust. Olivine crystallized throughout much of the crystallization of the mantle and may be present at many lunar mascon basins, where gravity measurements indicate that the lunar crust is thin and the mantle is close to the surface (Shearer et al., 1999; Yamamoto et al., 2010; Elkins-Tanton et al., 2011; Powell et al., 2012; Melosh et al., 2013; Miljković et al., 2015). The compositions of exposed olivine could provide clues to their origin. For example, the composition could reveal the existence of mantle overturn. Exposures of Mg-rich olivine at large impact basins could be evidence of overturned mantle cumulates. It is hypothesized that an unstable density gradient in the mantle, which was generated by crystallization of the magma ocean, caused it to overturn (Ringwood and Kesson, 1976). In the

post-overturn model of the lunar mantle, Mg# (molar Mg/(Mg+Fe)) increases towards the crust (Elkins-Tanton et al., 2011). Another possibility is that basin-impacts exposed Mg-suite plutons which are believed to have formed when mantle overturn caused magnesian olivine cumulates to mix with a residual KREEP (potassium, rare earth element, and phosphorus) layer and subsequently melted (Shearer and Papkie, 1999). Apollo samples include Mg-suite rocks, which have relatively high Mg# and trace element and KREEP concentrations.

Alternatively, olivine may be cumulates of shallow intrusions or mantle xenoliths that were transported magmatically to the surface by dikes. Analysis of stress states from lithospheric loading by maria suggests that the areas around large impact basins are particularly favorable for magma ascent via dikes (McGovern and Litherland, 2011). Furthermore, Andrews-Hanna et al. (2013) identified linear gravity anomalies that they interpreted to be ancient dikes. One of the largest proposed dikes is located at Crisium in the vicinity of previous olivine detections.

In this study, we used M^3 data to search for olivine at Crisium, Nectaris, and Humorum basins, which are three areas where Yamamoto et al. (2010) detected olivine. We also searched for olivine near Roche crater, where Andrews-Hanna et al. (2013) identified a possible dike similar to the one found at Crisium, which is associated with olivine (Yamamoto et al., 2010; Powell et al., 2012). Unlike Spectral Profiler, which Yamamoto et al. (2010) used for detecting olivine, M^3 is an imaging spectrometer that allows for a more spatially comprehensive investigation. Maps of topography and slope, created using LOLA data, GRAIL crustal thickness models, and WAC and NAC images allowed for us to put olivine detections into geologic context. Furthermore, previous studies did not quantitatively estimate olivine abundance. Here, we estimated Mg# and mineral abundances (olivine, orthopyroxene, clinopyroxene, and plagioclase) for each M^3 olivine spectrum using Hapke radiative transfer modeling.

Methods

We identified olivine at Crisium, Nectaris, and Humorum basins and near the crater Roche, using M^3 data. M^3 has spatial resolution of 140 m and, because it is an imaging spectrometer, allowed us to identify links between olivine spectra and geologic features. Along with high-spatial resolution the data are high spectral resolution, 85 bands from 460 to 2980 nm, which can be used to distinguish mineral signatures. We used level 2 M^3 reflectance data, which is thermally, geometrically, and photometrically corrected (Lundeen et al., 2012).

To identify olivine locations we used an olivine index based on the algorithm developed for the Compact Reconnaissance Imaging Spectrometer for Mars (CRISM) onboard the Mars Reconnaissance Orbiter but optimized for M^3 wavelengths (Pelkey et al., 2007). Olivine spectra have three overlapping absorption features at approximately 0.85, 1.05, and 1.25 μm, which

yield a composite absorption band centered near 1 µm (Fig. 1). The olivine index assigns a relative value to an M^3 pixel based on the depth of the 1-µm absorption as given by the equation:

$$olivine\ index = \left(\frac{R_{1695}}{0.1 * R_{1050} + 0.1 * R_{1210} + 0.4 * R_{1330} + 0.4 * R_{1470}}\right) - 1$$

where R is the reflectance measured at each M^3 wavelength given as a subscript in nm.

The algorithm is formulated to scale with olivine abundance, such that greater values indicate higher olivine concentrations. However, a number of factors beyond olivine abundance (e.g. grain size) influence the 1-µm absorption feature, and in turn influence the olivine index value. Thus, the olivine index is not a parameter from which an absolute quantitative value can be derived. Instead we used it as a qualitative indicator of the location and relative abundance of olivine. Applying the algorithm to the M^3 images reveals spatial variations of olivine abundance that can be matched to morphologic features.

To ensure that the algorithm identified olivine correctly, the spectra of pixels with high olivine index values were visually examined. In our olivine investigation, the absorption features of plagioclase and pyroxene were often superimposed on olivine spectra. Olivine has one broad composite absorption band centered near 1 µm. Plagioclase exhibits an absorption band centered at 1.25 µm. Pyroxene has an absorption band centered near 1 µm and an additional absorption band centered near 2 µm, which olivine lacks. Thus, the presence of plagioclase and/or pyroxene with olivine makes it difficult to quantitatively estimate olivine abundance by visual inspection. Hence we classified our spectra with a weak 2-µm band as olivine-dominated pyroxene mixtures, based on work by Singer (1981) that provided reflectance spectra for olivine-pyroxene mixtures. We classified olivine spectra without 2-µm absorptions as olivine spectra, regardless of any minor plagioclase that may be superimposed on the olivine spectra. We divided the spectra that are solely olivine into two groups based on composition: Mg-dominated and Fe-dominated. Fe-dominated olivine spectra have a deeper and more asymmetric 1-µm absorption band than Mg-dominated spectra (Fig. 1) (Burns, 1993).

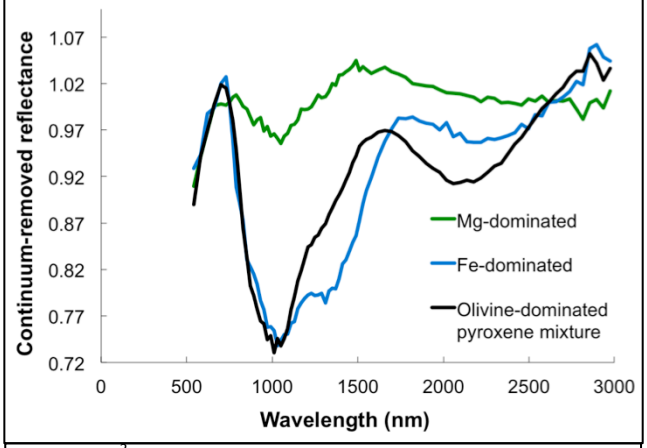

Figure 1: M^3 spectra from this study showing Mg-dominated and Fe-dominated olivines, and an olivine-dominated pyroxene mixture. Straight-line continuum removal at 750 and 2620 nm.

For our visually confirmed olivine spectra we used radiative transfer modeling to estimate the abundances of olivine, orthopyroxene, clinopyroxene, and plagioclase. Radiative transfer equations describe the scattering of light during interaction with surfaces, and can be used to model the reflectance spectra of mineral mixtures varying in grain size, chemistry, and space weathering effects (e.g. Hapke, 1981; 1993; 2001). Comparing modeled spectra to remote sensing spectra allows for the quantification of the mineral abundances of remote spectra. Before comparing modeled and remote spectra, we removed a straight-line continuum, tangential to the spectrum at 750 and 2500 nm, from each modeled spectrum and M^3 spectrum. The continuum is removed in order to remove the spectral slope, which is the change in reflectance with wavelength in the absence of spectral absorptions. 750 and 2500 nm were chosen as the continuum points, because they are located at opposite ends of the spectrum away from spectral absorptions. To derive compositions from our M^3 olivine exposures, we found the closest spectral match using the mean absolute difference in reflectance between the modeled spectra and the given M^3 spectrum.

The modeled spectra are part of a spectral library that is identical to those used by Lemelin et al. (2015), except calculated for M^3 specific wavelengths. Lemelin et al. (2015) compared modeled spectra to data from central peaks acquired by Kaguya's Multiband Imager, which includes nine bands in the ultraviolet-visible and near infrared. The library uses optical constants from Lucey (1998) and is refined with the Lunar Soil Characterization Consortium (LSCC) data by Lucey et al. (2014). We used a grain size of 17 μm, and the endmembers of the spectral libraries are all crystalline (Pieters et al., 1993). If shocked plagioclase were present in the remote spectra, the plagioclase abundance would be underestimated when comparing remote spectra with the library (Johnson and Hörz, 2003). The spectral library does not include ilmenite, but abundances of less that 15 wt% ilmenite do not affect the relative mineral abundance estimations (Lucey, 2004). Mafic mineral abundances were calculated in 10% abundance intervals from 0% to 100%, whereas plagioclase abundances are calculated at 1% abundance intervals. This gives a total of 6,601 compositions. Spectra were also computed for these mineral mixtures at seven different amounts of submicroscopic iron (SMFe), which includes the optical effects of two sizes of SMFe (Lucey and Riner, 2011). This gives a total of 46,207 modeled spectra. In addition, modeled spectra were computed at two different values of MgO/(MgO+FeO) (Mg#), 65 and 90. In total, we had 92,414 modeled spectra to compare to our remote spectra.

In an effort to constrain structural and magmatic evolution, we examined the geophysical settings of the four study regions using products produced from measurements of gravity by the GRAIL mission. We plotted maps of Bouguer gravity and crustal thickness using the model of Wieczorek et al. (2013) (Fig. 2). Maps of topography and slope were created using data from LOLA onboard LRO (Smith et al., 2010). WAC and NAC images from LRO allowed for

further observation of geologic settings (Robinson et al., 2010). Locations of olivine detections are displayed on WAC base maps (Fig. 4).

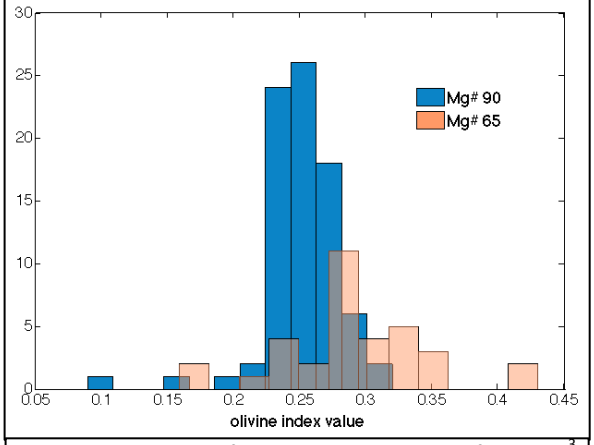

Figure 3: Histogram of the olivine index values for our M^3 olivine spectra with Mg# 90 and Mg# 65.

Results

We produced M^3 mosaics of our four study areas, Crisium, Nectaris, and Humorum basins and Roche crater. The CRISM olivine index algorithm was applied to each M^3 mosaic. With images of the olivine index data aiding the detection of olivine, we identified a total of 124 M^3 olivine spectra throughout the four study areas. A histogram of the olivine index values is shown in Figure 3.

Crisium

At Crisium basin we identified 62 spectra with signatures that represent olivine or olivine-dominated mixtures. These spectra are located on the rims of small craters, on massifs at the rim of Crisium, and on mare both inside and outside of Crisium basin. We were able to confirm many olivine locations that were detected by Yamamoto et al. (2010) and Powell et al. (2012), including Lacus Perseverantiae and a potential dike at Eimmart A. We report several olivine detections where olivine was previously undiscovered, including on the main basin-filling mare of Crisium. One such discovery is located on the rim and in the ejecta of Picard crater. Crustal thickness models based on GRAIL measurements by Wieczorek et al. (2013) and LOLA topography indicate that Picard crater is large enough to have penetrated through the thin crust. In contrast, the majority of our olivine detections correlate with crustal thickness maxima on the rim of Crisium.

Nectaris

Nearly all of the olivine detections at Nectaris are confined to the mare. Our investigation confirmed every olivine location detected by Yamamoto et al. (2010), including the rim and central peak of Theophilus. In addition, we were able to find many more olivine locations, for a total of 45 olivine spectra. Although crustal thickness inside Nectaris basin is as low as 5 km in some areas, none of the craters where olivine is found are large enough to have penetrated through the crust (Fig. 2).

Humorum

A total of 8 olivine spectra were detected at Humorum basin. In this investigation, only one of three olivine locations detected by Yamamoto et al. (2010) was confirmed. A new olivine discovery was made at Lee crater, where olivine appeared to be Fe-dominated. In addition, two Mg-dominated olivine spectra were found on a graben in northwest Humorum. All of the

olivine detections at Humorum are located on its rim.

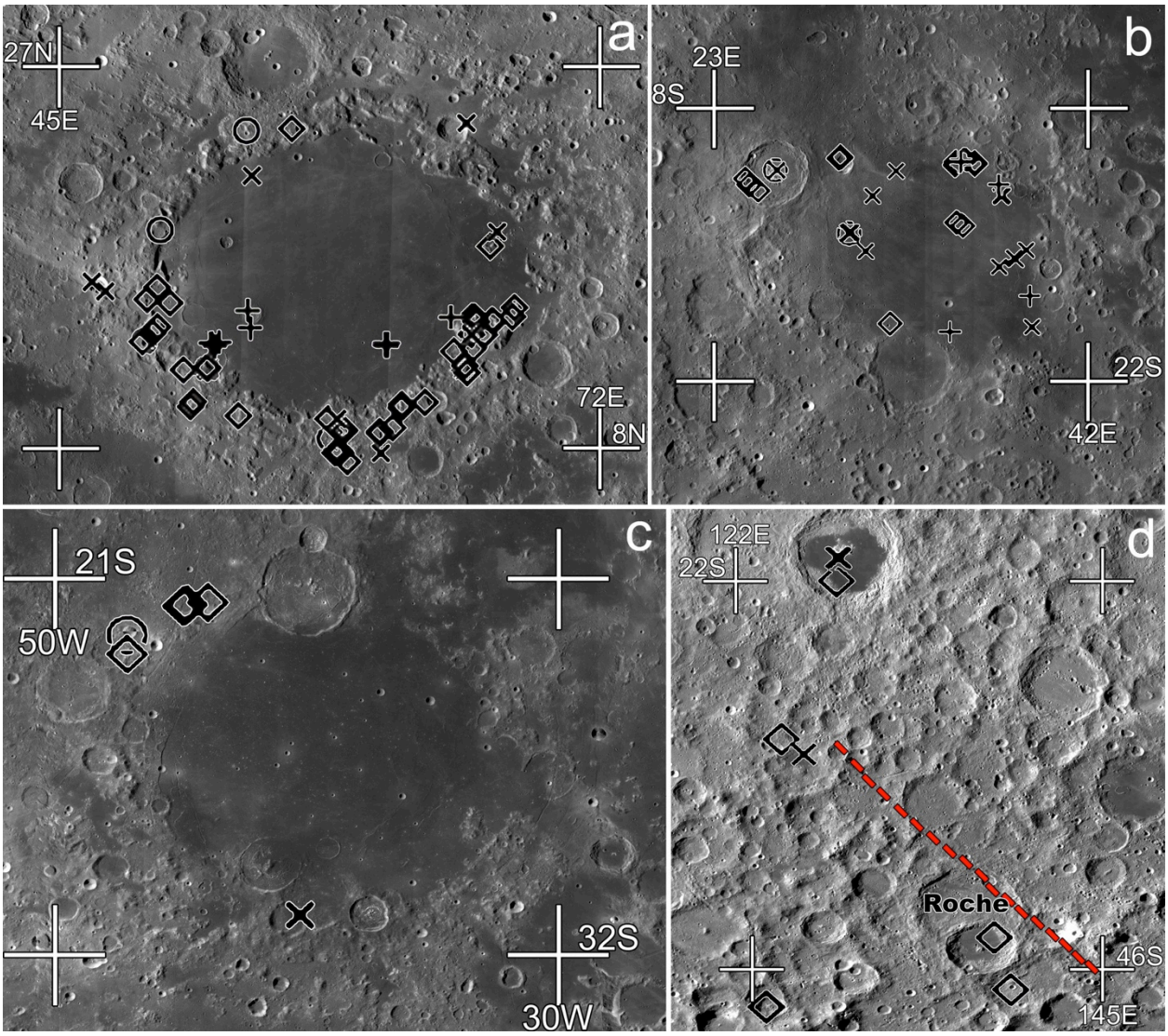

Figure 4: Locations of Fe-dominated olivine (×), Mg-dominated olivine (♢), and olivine-dominated pyroxene mixture (+) at (a) Crisium, (b) Nectaris, (c) Humorum basins, and (d) near Roche crater from this study. Detections from Yamamoto et al. (2010) are shown as circles. The approximate location of the linear gravity anomaly at Roche (d) is shown in red (Andrews-Hanna et al. 2013). Base maps are WAC images.

Roche

Roche, a 153-km diameter crater located on the lunar farside (42.2°S 136.3°E) at the edge of South Pole-Aitken (SPA) Basin, had not been previously investigated for olivine using high spectral resolution data. Andrews-Hanna et al. (2013) identified a linear gravity anomaly at Roche using GRAIL data, which they interpreted to be an ancient dike. We identified 9 olivine spectra near Roche. Several of our detections, both Fe-dominated and Mg-dominated spectra, were in close proximity to the proposed dike.

By comparing our olivine spectra with the modeled spectra, we found that mineral abundances vary greatly. Figure 5 shows a ternary diagram with estimated mineral abundances for the four study areas. At Crisium, the average olivine content of all 62 spectra is 20%. The maximum olivine content is 80%, located on a small crater in Lacus Perseverantiae. Spectra that we classified as olivine-dominated pyroxene mixtures by visual examination were indeed high in pyroxene, between 50 and 70%, but these spectra also had some of the highest olivine contents, averaging 34%. The average olivine abundance at Humorum is 27%, with a maximum of 44% olivine. At Nectaris, the average olivine abundance is 31% and the maximum is 67%. Roche has an average olivine abundance of 31% and a maximum of 48%.

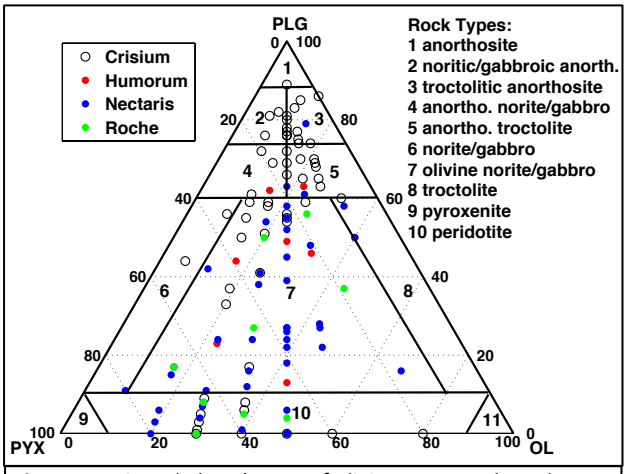

Figure 5: Mineral abundances of olivine spectra plotted on an olivine-plagioclase-pyroxene ternary diagram.

Discussion

Geophysical settings and estimated mineral abundances allow for the interpretation of the origins of exposed olivines and the mechanisms of transport to the lunar surface. Possible transport mechanisms include excavation of mantle or lower crustal material by basin-forming impact, or magmatic emplacement of cumulates or xenoliths. Furthermore, mineral abundances also provide insight into the lunar mantle overturn and the origin of olivine exposures.

Mantle excavation at Crisium

There is a diversity of origins for olivine located on the mare basalts within and around Crisium. Our examination of the geophysical setting at Crisium basin suggests that olivine exposed on the main mare at Picard crater may be primary olivine from the mantle. The crust inside Crisium basin is thin enough that the superposed 23-km diameter Picard crater likely penetrated through the crust, exposing mantle material. The estimated mineral abundances for the olivine spectra on the rim and in the ejecta of Picard crater indicate that these rocks are peridotites. Other olivine-rich areas are located on the rim of Crisium near local crustal thickness maxima, which may indicate that mantle material was excavated by the Crisium impact and deposited at the rim. If olivine on the rim of Crisium is indeed mantle olivine, the Mg-rich composition suggests that mantle overturn occurred (Elkins-Tanton et al., 2011). Estimated mineral abundances reveal that most of these rocks are troctolites and olivine-rich norites (Fig. 5), which is also consistent with an upper mantle disrupted by overturn. However, troctolites and olivine-rich norites are also consistent with Mg-suite rocks, which could have

been exposed by basin-impact. We estimated that the olivines on the rim of Crisium have an Mg# of 90, but Mg# alone cannot distinguish between the mantle and Mg-suite origins. Overturned olivine at the crust-mantle boundary is expected to have an Mg# of 90, whereas Mg-suite rocks exhibit a range in Mg# of about 70 to 90 (Taylor, 2009; Elkins-Tanton et al., 2011). Although Zhu et al. (2013) propose that a lower potassium concentration at the rim compared to the mare is the result of the redistribution of material from an exposed pluton, low thorium concentrations indicate that neither a KREEP layer nor Mg-suite pluton was excavated (Jolliff et al., 2000).

Magmatic emplacement

Magmatic processes, including dikes, also could have transported olivine located on the rim of Crisium. Consistent with Powell et al. (2012), we identified olivine on the rim of Eimmart A where there is morphologic evidence for a potential dike. In addition, olivine located at Lacus Perseverantiae were likely transported magmatically because here the crust is too thick for the craters where the olivine are detected to have penetrated to the mantle. These olivine exposures are unique compared to others at Crisium, because they are peridotites with the highest olivine abundances (60 and 80%) and are relatively Fe-rich (Mg# 65). These compositional differences suggest that they may be mantle xenoliths.

Olivine exposures in Nectaris basin are confined to the rims of small craters (<5 km diameter) on the mare. Although crustal thickness inside Nectaris basin is as low as 5 km in some areas, none of the craters where olivine is found are large enough to have penetrated through the crust and exposed mantle material. Instead, olivine-rich material was likely magmatically transported. Estimated mineral abundances reveal that the compositions are olivine-rich norites and peridotites, as well as a few troctolites. Many olivine-rich basalt Apollo samples are norites, but very few have compositions that are closer to that of peridotite or troctolite (Taylor et al., 1991). Thus, small craters on the Nectaris mare probably exposed a layer of olivine-rich mare basalt or a shallow intrusion beneath the mare.

At Humorum basin, the graben exhibiting olivine sites were likely created by extensional stresses caused by the loading of mare basalt (McGovern and Litherland, 2011; Hackwill et al., 2006). Extensional stresses would also have been favorable to the formation of dikes. Estimated compositions are olivine-rich norites and anorthosite-rich norites and troctolites. We conclude that olivines detected at the graben in northwest Humorum are likely cumulates of shallow intrusions.

Estimated mineral abundances of the Roche olivine spectra give compositions of peridotite and olivine-rich norite. Due to the thicker crust on the lunar farside, material exposed near Roche crater is not likely to be impact-exposed mantle. However, the presence of

olivine at this location suggests that magmatic intrusions reached the shallow subsurface and were exposed by small impacts, consistent with the geophysically inferred presence of a dike near Roche. Considering that Roche crater lies on the edge of SPA Basin, it is worth noting that Yamamoto et al. (2012) identified olivine-rich material in the outer regions of SPA Basin in the central peaks or peak rings of Schrödinger basin and Zeeman crater. We detected olivine at several sites around Roche, including on the central peak of nearby Tsiolkovsky carter. Yamamoto et al. (2012) hypothesized that the SPA basin-forming impact melted a large amount of the lunar upper mantle and crust, and distributed the melted materials to the outer region where local differentiation hid olivine-rich materials until they were excavated by Schrödinger basin and Zeeman crater. They suggest that space weathering and regolith gardening obscured olivine spectra, only to be revealed now by landslides or small-scale impacts. For our olivine detections near Roche, we acknowledge that a similar set of events may have occurred to expose olivine-rich material associated with SPA Basin.

Conclusions

High-resolution, thermally and photometrically corrected data from M^3 coupled with Hapke radiative transfer model have allowed for estimation of mineral abundances of olivine-rich material at Crisium, Humorum, and Nectaris basins and near Roche crater. Modeled GRAIL crustal thickness from Wieczorek et al. (2013), LOLA topography maps, and WAC and NAC images were used to examine the geophysical and morphologic settings and put our olivine locations into geologic context. Crustal thicknesses at Nectaris and Humorum basins and Roche crater indicate that olivines were transported by magmatic processes. At Humorum basin, olivine sites on graben indicate magmatic transport, likely the result of loading of mare basalt creating extensional stresses favorable to the formation of dikes. In addition, detections of peridotites and olivine-rich norites at Roche crater are consistent with the presence of a dike. Olivine exposures in Nectaris basin are confined to the rims of small craters that penetrated the mare, probably exposing an olivine-rich mare basalt or shallow intrusion beneath the mare. There is a diversity of olivine-bearing lithologies at Crisium. Mantle olivine may have been exposed by the basin-forming impact and deposited on the rim of Crisium and by Picard crater, which likely penetrated through the mare and the extremely thin crust. Assuming olivine on the southern rim of Crisium is from the mantle, the Mg-dominated composition indicates that mantle overturn occurred. In addition, peridotites of up to 80% olivine at Lacus Perseverantiae are possible mantle xenoliths. Overall, our findings identify possible origins and transport mechanisms of the exposed olivine, providing insight to the structural and magmatic evolution of the Moon.

References

Andrews-Hanna, J. C., Asmar, S. W., Head, J. W., Kiefer, W. S., Konopliv, A. S., Lemoine, F. G., ... & Zuber, M. T. (2013). Ancient igneous intrusions and early expansion of the Moon revealed by GRAIL gravity gradiometry. *Science*, *339*(6120), 675-678.

Burns, R. G. (1993). *Mineralogical applications of crystal field theory* (Vol. 5). Cambridge University Press, New York.

Elkins-Tanton, L. T., Burgess, S., & Yin, Q. Z. (2011). The lunar magma ocean: Reconciling the solidification process with lunar petrology and geochronology. *Earth and Planetary Science Letters*, *304*(3), 326-336.

Hackwill, T., Guest, J., & Spudis, P. (2006). Stratigraphy and evolution of basalts in Mare Humorum and southeastern Procellarum. *Meteoritics and Planetary Science*, *41*, 479-488.

Hapke, B. (1981). Bidirectional reflectance spectroscopy: 1. Theory. *Journal of Geophysical Research: Solid Earth (1978–2012)*, *86*(B4), 3039-3054.

Hapke, B. (1993). *Theory of Reflectance and Emittance Spectroscopy*, Topics in Remote Sensing (No. 3), Cambridge University Press, New York.

Hapke, B. (2001). Space weathering from Mercury to the asteroid belt. *Journal of Geophysical Research: Planets (1991–2012)*, *106*(E5), 10039-10073.

Johnson, J. R., & Hörz, F. (2003). Visible/near-infrared spectra of experimentally shocked plagioclase feldspars. *Journal of Geophysical Research: Planets (1991–2012)*, *108*(E11).

Jolliff, B. L., Gillis, J. J., Haskin, L. A., Korotev, R. L., & Wieczorek, M. A. (2000). Major lunar crustal terranes: Surface expressions and crust-mantle origins. *Journal of Geophysical Research: Planets (1991–2012)*, *105*(E2), 4197-4216.

Lemelin, M., Lucey, P. G., Song, E., & Taylor, G. J. (2015). Lunar central peak mineralogy and iron content using the Kaguya Multiband Imager: Reassessment of the compositional structure of the lunar crust. *Journal of Geophysical Research: Planets, 120.*

Lucey, P. G. (1998). Model near-infrared optical constants of olivine and pyroxene as a function of iron content. *Journal of Geophysical Research: Planets (1991–2012)*, *103*(E1), 1703-1713.

Lucey, P. G. (2004). Mineral maps of the Moon. *Geophysical Research Letters*, *31*(8).

Lucey, P. G., & Riner, M. A. (2011). The optical effects of small iron particles that darken but do not redden: Evidence of intense space weathering on Mercury. *Icarus*, *212*(2), 451-462.

Lucey, P. G., Norman, J. A., Crites, S. T., Taylor, G. J., Hawke, B., Lemelin, M., & Melosh, H. J. (2014). A large spectral survey of small lunar craters: Implications for the composition of the lunar mantle. *American Mineralogist*, *99*(11-12), 2251-2257.

Lundeen S. et al. (2012). M3 AV-SIS, v. 3.17, JPL D-38529.

McGovern, P. J., & Litherland, M. M. (2011). *Lunar and Planetary Science XLII, 42,* Abstract #2587.

Melosh, H. J., Freed, A. M., Johnson, B. C., Blair, D. M., Andrews-Hanna, J. C., Neumann, G. A., ... & Zuber, M. T. (2013). The origin of lunar mascon basins. *Science*, *340*(6140), 1552-1555.

Miljković, K., Wieczorek, M. A., Collins, G. S., Solomon, S. C., Smith, D. E., & Zuber, M. T. (2015). Excavation of the lunar mantle by basin-forming events on the Moon. *Earth and Planetary Science Letters, 409,* 243-251.

Pieters, C. M., Fischer, E. M., Rode, O., & Basu, A. (1993). Optical effects of space weathering: The role of the finest fraction. *Journal of Geophysical Research: Planets (1991–2012)*, *98*(E11), 20817-20824.

Pelkey, S. M., Mustard, J. F., Murchie, S., Clancy, R. T., Wolff, M., Smith, M., ... & Gondet, B. (2007). CRISM multispectral summary products: Parameterizing mineral diversity on Mars from reflectance. *Journal of Geophysical Research: Planets (1991–2012)*, *112*(E8).

Powell, K. E., McGovern, P. J., & Kramer, G. Y. (2012). Olivine detections at the rim of Crisium basin with Moon Mineralogy Mapper. *Lunar and Planetary Science XLIII, 43,* Abstract #1689.

Ringwood, A. E., & Kesson, S. E. (1976). A dynamic model for mare basalt petrogenesis. *In Lunar and Planetary Science Conference Proceedings, 7,* 1697–1722.

Robinson, M. S., Brylow, S. M., Tschimmel, M., Humm, D., Lawrence, S. J., Thomas, P. C., ... & Hiesinger, H. (2010). Lunar reconnaissance orbiter camera (LROC) instrument overview. *Space Science Reviews, 150(1-4),* 81-124.

Shearer, C. K., & Papike, J. J. (1999). Magmatic evolution of the Moon. *American Mineralogist*, *84*, 1469-1494.

Singer, R. B. (1981). Near-infrared spectral reflectance of mineral mixtures: Systematic Combinations of pyroxenes, olivine, and iron oxides. *Journal of Geophysical Research: Solid Earth (1978–2012)*, *86*(B9), 7967-7982.

Smith, D. E., Zuber, M. T., Neumann, G. A., Lemoine, F. G., Mazarico, E., Torrence, M. H., ... & Bartels, A. E. (2010). Initial observations from the lunar orbiter laser altimeter (LOLA). *Geophysical Research Letters*, *37*(18).

Taylor, G. J., Warren, P., Ryder, G., Delano, J., Pieters, C., & Lofgren, G. (1991). Lunar rocks. *Lunar Sourcebook,* 183-284.

Taylor, G. J. (2009). Ancient lunar crust: Origin, composition, and implications. *Elements*, *5*(1), 17-22.

Wieczorek, M. A., Neumann, G. A., Nimmo, F., Kiefer, W. S., Taylor, G. J., Melosh, H. J., ... & Zuber, M. T. (2013). The crust of the Moon as seen by GRAIL. *Science*, *339*(6120), 671-675.

Yamamoto, S., Nakamura, R., Matsunaga, T., Ogawa, Y., Ishihara, Y., Morota, T., ... & Haruyama, J. (2010). Possible mantle origin of olivine around lunar impact basins detected by SELENE. *Nature Geoscience*, *3*(8), 533-536.

Yamamoto, S., Nakamura, R., Matsunaga, T., Ogawa, Y., Ishihara, Y., Morota, T., ... & Haruyama, J. (2012). Olivine-rich exposures in the South Pole-Aitken basin. *Icarus*, *218*(1), 331-344.

Zhu, M. H., Chang, J., Ma, T., Ip, W. H., Fa, W., Wu, J., ... & Tang, Z. (2013). Potassium Map from Chang'E-2 Constraints the Impact of Crisium and Orientale Basin on the Moon. *Scientific reports*, *3*.